


RESEARCH ARTICLE

Open Access



Multi-scale X-ray tomography and machine learning algorithms to study MoNi₄ electrocatalysts anchored on MoO₂ cuboids aligned on Ni foam

Emre Topal^{1,2*} , Zhongquan Liao³, Markus Löffler^{1,2}, Jürgen Gluch³, Jian Zhang^{1,4}, Xinliang Feng^{1,4} and Ehrenfried Zschech^{1,2,3}

Abstract

For a systematic materials selection and for design and synthesis of systems for electrochemical energy conversion with specific properties, it is essential to clarify the general relationship between physicochemical properties of the materials and the electrocatalytic performance and stability of the system or device. The design of highly performant and durable 3D electrocatalysts requires an optimized hierarchical morphology and surface structures with high activity. A systematic approach to determine the 3D morphology of hierarchically structured materials with high accuracy is described, based on a multi-scale X-ray tomography study. It is applied to a novel transition-metal-based materials system: MoNi₄ electrocatalysts anchored on MoO₂ cuboids aligned on Ni foam. The high accuracy of 3D morphological data of the formed micro- and nanostructures is ensured by applying machine learning algorithms for the correction of imaging artefacts of high-resolution X-ray tomography such as beam hardening and for the compensation of experimental inaccuracies such as misalignment and motions of samples and tool components. This novel approach is validated based on the comparison of virtual cross-sections through the MoNi₄ electrocatalysts and real FIB cross-sections imaged in the SEM.

Keywords: X-ray computed tomography, Machine learning, Nanoparticles, 3D morphology, Electrocatalyst, Energy conversion

Introduction

The development of technologies for the efficient use of renewable energies has become a research priority worldwide. For advanced electrochemical energy conversion devices such as rechargeable metal–air batteries, regenerated fuel cells and water splitting devices, high-performance and low-cost non-precious metal catalysts are of critical importance for pertinent electrochemical

processes like oxygen reduction reaction (ORR), oxygen evolution reaction (OER) and hydrogen evolution reaction (HER) [1].

A wide range of materials, especially various transition-metal (TM) based materials (e.g., Fe-, Co-, Mo-, Ni-, V-, Cu-based precursors) and metal-free carbon materials, have been regarded as promising economical and efficient replacements to conventional, expensive precious-metal-based materials (e.g., Pt-, Pd-, Ir-, Au-, Ag-, Ru-based precursors). Some of these advanced electrocatalytically active materials outperform conventional precursors, particularly considering properties like electrocatalytic activity and long-term stability

*Correspondence: emre.topal@tu-dresden.de

¹ Center for Advancing Electronics Dresden, Technische Universität Dresden, Dresden, Germany

Full list of author information is available at the end of the article



[1–3]. However, further systematic studies are needed to guarantee an efficient and durable operation during the requested lifetime of an energy conversion device.

Among the TMs, Ni and Mo have emerged as potential constituents because of their unique electronic properties and anticipated synergetic effects to alter significantly surface properties of materials to favor electrolysis. Ni atoms are characterized by a high reactivity (Ni > Co > Fe > Mn), which is governed by the bond strength of OH–M^{2+δ}, with 0 ≤ δ ≤ 1.5, energetics (Ni < Co < Fe < Mn), a trend which is independent of the source of the OH, i.e., either the supporting electrolyte (for the OER) or the water dissociation product (for the HER) [4]. Mo atoms have superior adsorption properties towards hydrogen. Consequently, Ni- or Mo-based electrocatalysts in the shape of alloys, nitrides, carbides, borides, phosphides, sulfides, selenides, oxides, hydroxides and metal-organic frameworks (MOFs) [5] have been studied recently (see review [1]). Many of them have shown promising electrocatalytic activity towards ORR, OER and HER, as monofunctional or bifunctional materials. Particularly, reactivity and hydrogen adsorption are high for Mo_xNi_y-based electrocatalysts [6].

For a systematic materials selection and for design and synthesis of systems for electrochemical energy conversion with specific properties, it is essential to clarify the general relationship between physicochemical properties of the materials and the electrocatalytic performance and stability of the system or device. The following three aspects are important [7]:

- Firstly, the intrinsic properties of a component determine its activity and conductivity. Rational selection of components is beneficial for reducing overpotentials and Tafel slopes, and for increasing catalytic current density. Meanwhile, the incorporation of conductive components facilitates fast electron transfer.
- Secondly, modification of the material's morphology selectively exposes specific crystal faces with higher activity.
- Thirdly, the 3D porous structure with high surface area can provide abundant active sites because favorable structures contribute to preventing agglomeration and can promote mass transfer (i.e., reactant diffusion and product release).

The high electrocatalytic efficiency of Mo–Ni-based alloy (Mo_xNi_y) electrocatalysts for HER is based on their advantageous surface chemistry, i.e., the crystalline structure of the materials and the chemical bonding (to improve intrinsic surface properties). The energy barrier of the prior Volmer step (electron-coupled water dissociation for the formation of adsorbed hydrogen)

is significantly reduced for these alloys, and—because of the reduced Tafel slope—the subsequent Tafel-step determined HER process (combination of adsorbed hydrogen into molecular hydrogen) is accelerated under alkaline conditions [4].

In addition to the intrinsic properties of the constituent components, the materials' morphology is another crucial factor in designing high-performance electrocatalysts, as it closely correlates with exposed facets and active sites [8–10]. The design of robust 3D electrocatalysts with an optimized hierarchical morphology and surface structures with high activity, resulting in highly performant and durable systems, is a task that is expected to play an increasing role in the future [11]. Advanced electrocatalysts have to be designed in a way that the total number of accessible active sites and the intrinsic activity of each active site is high [12–16]. The morphology of such hierarchically designed systems and respective materials can be tailored, e.g., by precursor templates with a high specific surface area and well-designed pore topology as well as nanosized electrochemically active particles (to increase the number of active catalytic sites) and with high ion diffusion (to improve the reaction kinetics). However, these nanostructures are intrinsically less stable than bulk metals or oxides [17, 18]. Therefore, their morphology has to be optimized balancing efficiency and electrochemical stability. On the other hand, improving reaction kinetics will convey an operation at lower overpotentials for the same hydrogen production rate with beneficial effects on the durability [19]. Systems with a narrow size distribution of nano-sized particles, exposed electrocatalytically active edges and corners as well as the availability of internal and external surfaces in the hierarchical 3D system, provide enhanced ion diffusion, improved activity and reasonable durability [20].

A hierarchical nanoarray grown on free-standing electrode structures offers many advantages for the development of new electrocatalyst systems [21]. These hierarchically grown nanoarrays exhibit high open volume (porosity), high surface area, and uneven surface characteristics which enables to achieve a high density of catalytic active site [22, 23]. Furthermore, these unique morphological traits can provide another captivating property known as superaerophobicity [24]. In-time repelling ability to as-generated gas bubbles from the surface of the electrode allows a larger contact between electrode and electrolyte which accelerates the mass transfer [24, 25]. Additionally, superaerophobic behavior reduces the ohmic drop by alleviating the adhesion of as-formed gas bubbles on the electrode during the electrocatalytic process [26].

Ni foam supported MoNi₄ nanoparticles [6], 3D MoNi nanowires [27] and porous MoNi alloys [28] significantly

improved the HER activity. That means that bicontinuous and monolithic 3D electrode catalysts provide high reaction kinetics. Recently, we demonstrated an efficient hydrogen production on MoNi₄ electrocatalysts with fast water dissociation kinetics by anchoring numerous MoNi₄ nanoparticles on MoO₂ cuboids that are aligned on a conductive Ni foam [6]. Ni- and Mo-based oxides/hydroxides were used for the construction of hierarchical P-doped Ni(OH)₂/NiMoO₄ Ni(OH)₂ nanosheet arrays that were grown on Ni foam [21]. This electrocatalyst exhibited superior HER activity with a small overpotential and a low Tafel slope, and it can act also as an integrated electrocatalyst towards overall water splitting with a cell voltage of only 1.55 V to achieve a current density of 10 mA cm⁻² [21].

To develop and synthesize highly active and durable electrocatalyst materials, and particularly, to accelerate their reaction kinetics, most of the published papers analyze the surface activity of the materials. Crystalline structure, (surface) valence states of the cations and chemical bonding of the advanced electrocatalytically active materials are characterized using X-ray diffraction (XRD) [29], transmission electron microscopy (TEM) [30], X-ray photoelectron spectroscopy (XPS) [31] and X-ray absorption spectroscopy (XAS) [32].

The morphology of the formed nanostructures determines quantities like total surface area of the electrocatalytic active material and fluid dynamics, which has to be controlled during the formation process because these quantities determine the total activity and durability of the materials and consequently the operational performance and system stability. So far, the total surface area is often determined using the Brunauer–Emmett–Teller (BET) method, and the morphology of the nanostructures is usually discussed based on scanning electron microscopy (SEM) and TEM images, depending on the size of the structures and features to be imaged. These 2D images provide shape information about the formed nanostructures, however, the particle size distribution cannot be determined easily for most of the types of morphology of nano-sized particles (see e.g., [19]). In some cases, an estimate of the average crystal size of the material can be derived from the broadening of XRD lines. Detailed 3D information about the morphology of

the advanced electrocatalytically active materials that is needed to correlate with parameters that describe the performance and durability of electrocatalysts can be derived from tomography studies. Depending on the typical size of the studied objects, i.e., the electrocatalyst materials and the supporting structures, and the features of interest, electron tomography (ET) in the TEM or X-ray computed tomography (XCT), both nano-XCT and micro-XCT, are suitable technique to provide the morphology of the (sub-)structures of the electrocatalytically active materials [33].

Multi-scale tomography is an approach that combines the 3D image information at several hierarchical levels (typical feature size of structures). In Table 1, typical values for field-of-view (FOV) and spatial resolution are given for several tomography techniques. Given the typical resolution limits of X-ray computed tomography techniques in order to fully resolve the 3D morphology of hierarchical levels of a complex system, the combination of several techniques with different sample volume and resolution is required.

Nondestructively obtained 3D tomographic images of an object are generated by acquiring many projection images of a static object at several projection angles, and subsequently, by applying a reconstruction algorithm to these images. The limited-angle tomography approach (incomplete set of 2D images) [34], usually applied for electron tomography studies in the TEM because thinned lamellae are investigated, produces artefacts. In addition, artefacts caused by thermomechanical instability of tool components and sample motion, center of rotation misalignment and imperfections in the detector such as offset (geometrical shift of the detector grid) can occur in all types of tomography [35]. However, unavoidable misalignment and thermomechanical effects are more critical for imaging techniques with high spatial resolution, i.e., electron tomography in the TEM and nano-XCT in the transmission X-ray microscope (TXM). Therefore, for high spatial resolution tomography techniques, it is necessary but practically difficult or impossible to align the various system components with sub-micron precision. Therefore, the acquired projections usually do not match strictly the acquisition geometry as defined in the reconstruction algorithm. Consequently, the artefacts in

Table 1 Comparison of X-ray computed tomography techniques

Method	FOV	Spatial resolution	Energy	Sample thickness
Micro-XCT	0.5–50 mm	30–0.7 μm	30–160 kV	0.5–70 mm
Laboratory nano-XCT	10–100 μm	30–100 nm	5–20 keV	50 μm–10 mm
Synchrotron radiation nano-XCT	5–100 μm	10–100 nm	0.1–20 keV	1 μm–10 mm
ET/TEM	< 1–10 μm	< 1 Å	1 keV–1 MeV	< 150 nm

the reconstructed images are an unwanted consequence of this mismatch. The image artifact can be defined as any variation between the reconstructed values in an image and the true attenuation coefficients of the object. Since image artifacts can seriously degrade the quality of the reconstructed image it is critical to understand the reasons behind the artifacts and how to prevent or to suppress them to minimize the variation between the reconstructed values in an image and the true attenuation coefficients of the object. The Image reconstruction appears as be a powerful domain to address the issues of accuracy of the XCT technique.

In this work, we demonstrate how the 3D morphology of electrocatalyst supporting structures can be determined using micro-XCT and nano-XCT, including the application of machine learning algorithms for the generation of 3D geometrical data of the formed micro- and nanostructures with high accuracy. The obtained 3D reconstructed volumes are used to describe hierarchical structures. This multi-scale approach is proven for MoNi₄ electrocatalysts anchored on MoO₂ cuboids aligned on the conductive Ni foam.

Results

Micro-XCT

For the projections acquired from micro-XCT, the reconstruction was performed using the Feldkamp–Davis–Kress (FDK) algorithm [36]. The imperfections in the acquired data were corrected by the procedure explained in methods section (Fig. 9). The size of the reconstructed volume is 1994³ voxels and the voxel size is 0.44 μm. Reconstructed virtual cross-section images were taken after each step of the applied correction algorithm in Fig. 1. The proposed methodology successfully improved the reconstruction quality and effectively suppressed the artefacts. The center of rotation and the detector offset were calculated as −3.6 μm and −44.6 μm, respectively. The visible ring artefacts that are associated with the defective and/or underperforming detector elements were eliminated from the reconstructed image after applying this correction. The motion compensation effectively suppresses the motion artefacts that occur as streaks and blur.

The obtained 3D volume information allowed us to describe the morphology of Ni foam and the attached MoO₂ cuboids. The MoO₂ cuboids grown vertically on the surface of Ni foam. Their shapes are resolvable from the reconstructed 3D volume as shown in Fig. 2.

Nano-XCT

For the projections acquired from nano-XCT, the reconstruction was performed using the Filtered-Back-Projection (FBP) algorithm [37]. In order to improve the quality

of the acquired data, the workflow (Fig. 9) was applied as explained in the XCT image reconstruction section. The reconstructed virtual cross-section images from laboratory and from synchrotron radiation nano-XCT data are shown after each step of the applied correction algorithms in Figs. 3 and 4, respectively.

The size of the reconstructed volume from data acquired using the laboratory nano-XCT tool is 512³ voxels and voxel size is 31.9 nm. The center of rotation and the detector offset were calculated as −1.1 μm and −13.8 μm, respectively. The visible ring artefacts that are associated with the defective and/or underperforming detector elements were eliminated from the reconstructed image after the applied correction. The motion compensation effectively suppresses the motion artefacts that occur as streaks and blur (see Fig. 3). The applied correction methodology drastically improved the reconstruction quality compared to the prior step by finding correct voxel position-intensity correspondence.

The nano-XCT investigation allowed us to image MoO₂ micro cuboids grown vertically on the surface of Ni foam. As shown in Fig. 5, these needle-like MoO₂ micro cuboids are randomly spread over the surface of Ni foam. Their lengths vary between 10 to 20 μm. The laboratory nano-XCT investigation failed to resolve MoNi₄ particles on MoO₂ micro cuboids.

For the synchrotron radiation nano-XCT investigation, the size of the reconstructed volume was 541³ voxels, and the voxel size 9.4 nm. The applied new methodology effectively suppressed artefacts. The center of rotation and the detector offset were calculated as 2.9 nm, and 3.8 nm, respectively. No center of rotation related ring artefacts were visible in the reconstructed image due to the negligibly small misalignment on the system. Because the main deterioration resulted from the motion, edge artefacts on MoO₂ cuboids suppressed applying motion compensation (see Fig. 4).

The investigation of the MoNi₄/MoO₂@Ni composite using synchrotron radiation nano-XCT enables to resolve the single MoO₂ micro cuboids, and it allows imaging of the anchored MoNi₄ electrocatalytically active nano-sized particles on a MoO₂ micro cuboid as shown in the Fig. 6. The sizes of the round shaped MoNi₄ nanoparticles varies in the range of 20 to 100 nm.

Validation of the data

During the reconstruction of the acquired data, a series of correction steps including statistical minimization and machine learning was applied in order to suppress artefacts and to obtain highly accurate reconstructed data. To make sure that the applied correction algorithms do not introduce additional artifacts into reconstructed images, a validation test has to be performed. The applied

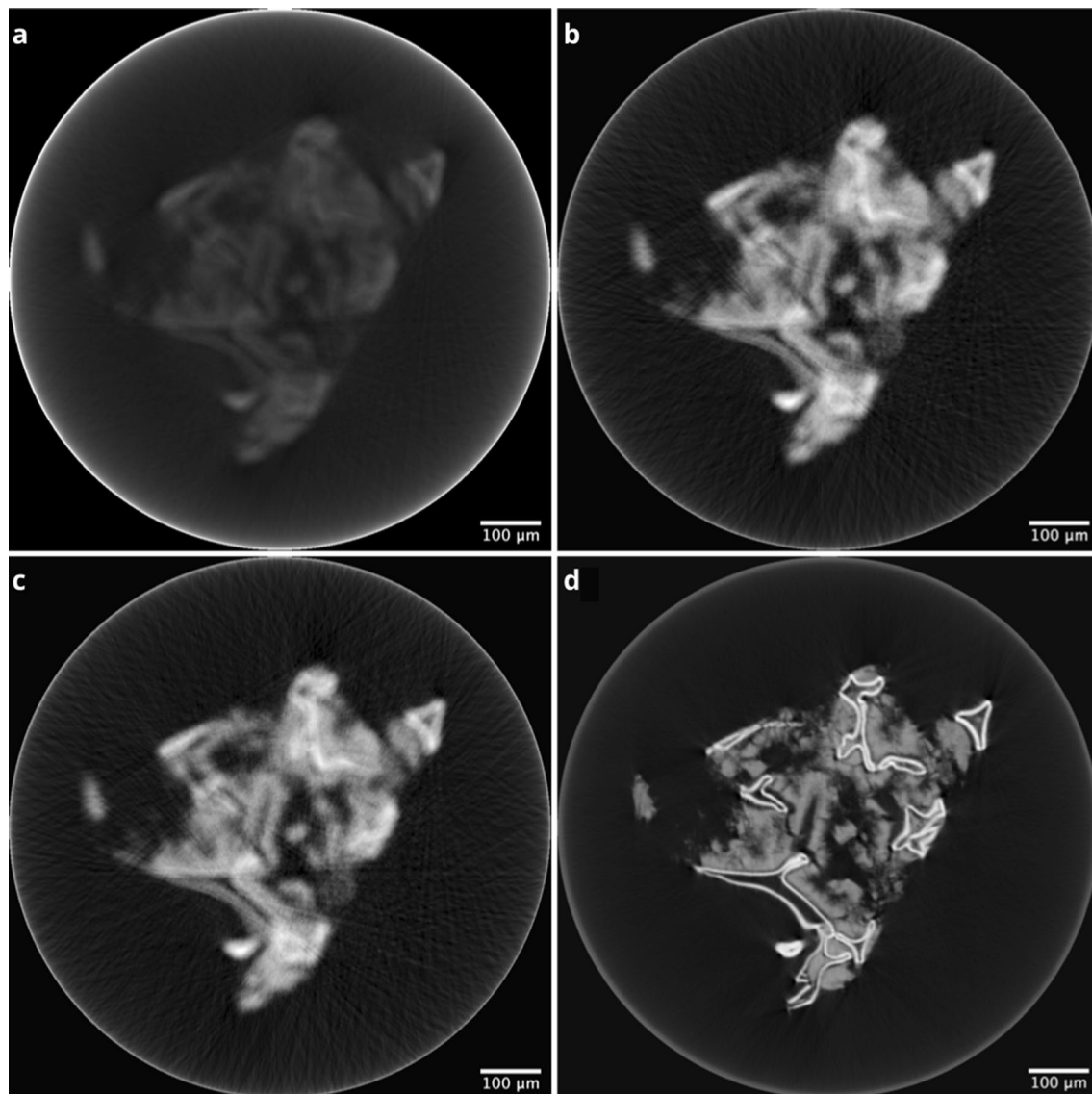
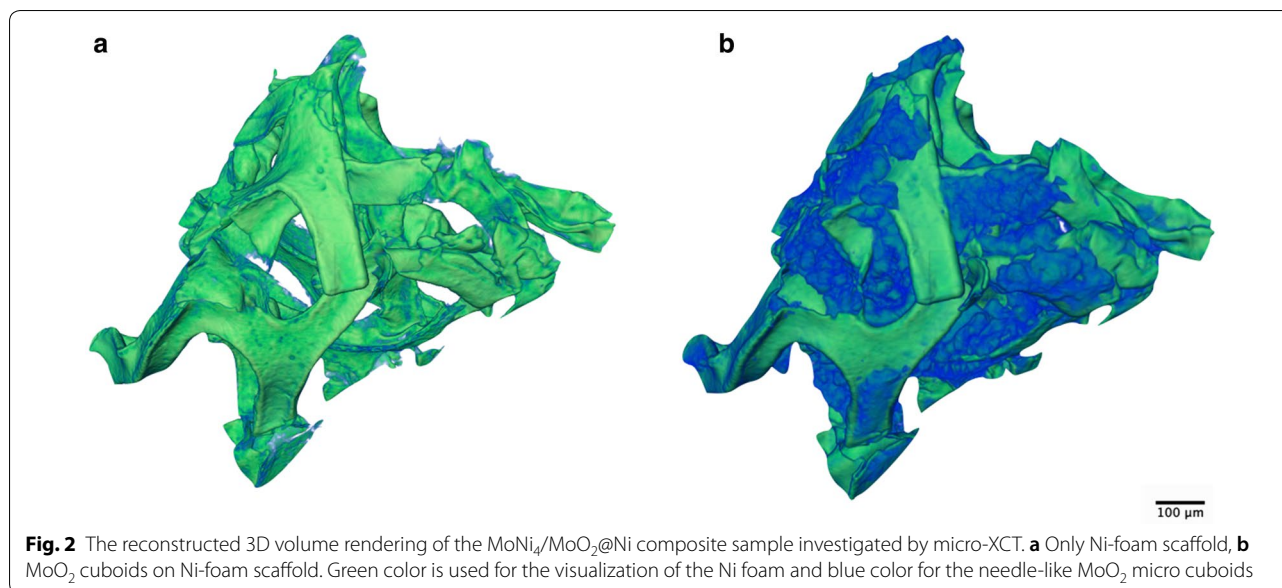


Fig. 1 The reconstructed virtual cross section of the $\text{MoNi}_4/\text{MoO}_2@Ni$ composite sample investigated by micro-XCT. The hollow white lines are the Ni foam scaffold and the grey zones are MoNi_2 oxide cuboids. The MoNi_4 nanoparticles are not resolvable in the micro-XCT study. The proposed reconstruction procedure is applied using the FDK algorithm. **a** Prior to the correction procedure, **b** after the beam-hardening correction/intensity adjustment, **c** after detector offset and center of rotation correction, and **d** after final motion compensation

correction algorithms are identically for the analysis of the data from all 3 XCT investigations—micro-XCT, laboratory nano-XCT and SR nano-XCT—and they do not depend on the studied sample volume and the resolution. Therefore, it is sufficient to perform the validation test for one XCT data set only.

The validation of the reconstructed data, i.e., the virtual cross-sections, was performed applying the focused ion beam (FIB) serial sectioning technique and subsequent imaging of the series of cross-sections in the SEM with nanometer resolution. This destructive procedure was

applied to the sample used for the nano-XCT experiment. The comparison of the virtual cross-sections from the reconstructed 3D volume and the real cross-sections from FIB/SEM is provided in Fig. 7. In order to obtain cross-section images (Fig. 7, center), subsequent SEM images are subtracted, and the comparison given for same ROI with nano-XCT at the same z-slice range. Considering the typical design of FIB/SEM tools and particular the angle between electron and ion columns, the SEM images are obtained with a tilt angle of 52° , i.e. virtual cross-section and real cross-section views may



differ due to fact that the acquired images in the SEM are side view projections. On the other hand, the positions are consistent as shown with arrows in Fig. 7. The thin pillar with an irregular arrangement, as shown with red arrow in Fig. 7, has a contrast difference with the other pillar due to its size, it is only seen as black dot in the virtual cross-section. Due to tilting of the SEM stage planar sectioning of this thin pillar is observed in the FIB cross-section. In addition, at the end point of the thin pillar, the positions of another non-vertically aligned pillar and another vertically aligned cuboid pillar, shown with blue and green arrows in the Fig. 7, respectively, supports our assessment. That means, since the arrangement of features in both cross-sections, the virtual cross-section based on nano-XCT data and the real FIB cross-section, are matching well, the methodology of data analysis as described in this paper, using machine learning algorithms, is validated.

Discussion

The advanced reconstruction of multi-scale tomography data provides comprehensive 3D information about the hierarchical structure of the studied electrocatalyst system: MoNi₄ electrocatalysts anchored on MoO₂ cuboids aligned on conductive Ni foam. The 3D morphology of electrocatalyst supporting structures as determined using micro-XCT and nano-XCT provide the following findings:

- The micro-XCT images clearly resolve the Ni foam and the attached needle-like MoO₂ micro cuboids.

- Using the laboratory nano-XCT technique, the MoO₂ micro cuboids were imaged. The MoO₂ micro cuboids are vertically arranged on the Ni foam, and the lengths of these cuboids are in the range of 10–20 μm with a rectangular cross-section of 0.5 × 1 μm².
- MoNi₄ nanoparticles positioned on one single MoO₂ cuboid were imaged using synchrotron radiation nano-XCT. The MoNi₄ nanoparticles are anchored on the MoO₂ cuboid. The sizes of these round shaped MoNi₄ nanoparticles are in the range of 20–100 nm.

The applied multi-scale tomography approach enables one to provide 3D information on the hierarchical morphology of the MoNi₄/MoO₂@Ni composite system nondestructively. Furthermore, the obtained 3D morphological data can be used to characterize size distribution and shape of cuboids and nano-sized particles to tailor the hierarchical morphology.

The application of machine learning algorithms allowed us to generate 3D geometrical data of the formed micro- and nanostructures with high accuracy. The developed reconstruction software, empowered by machine learning algorithms, significantly improved the reconstruction quality of the acquired data for both micro-XCT using cone-beam geometry and nano-XCT using parallel-beam geometry. The applied correction procedure effectively suppressed beam hardening effects, detector offset and center of rotation misalignment artefacts and motion during the XCT acquisition process.

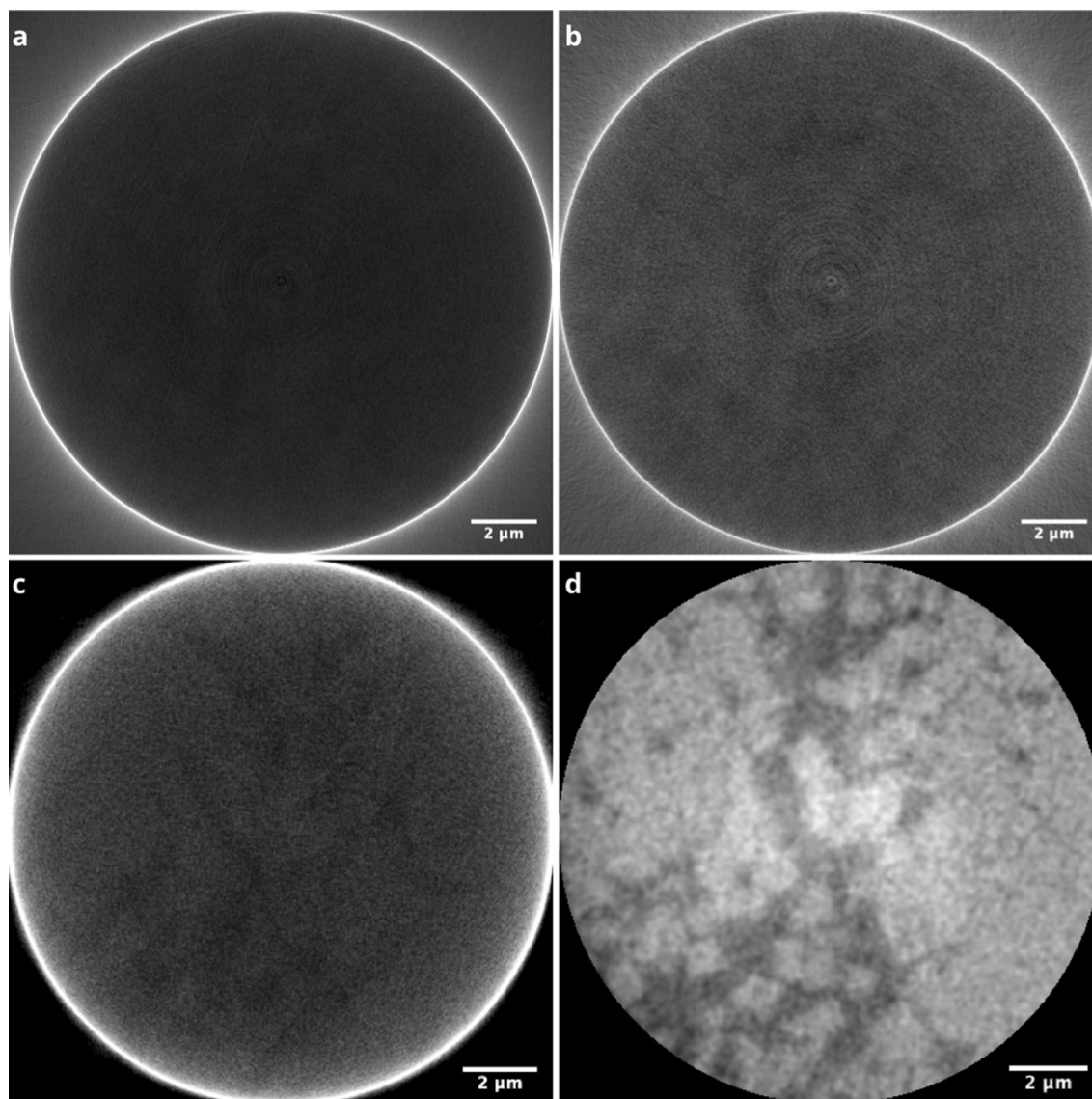


Fig. 3 The reconstructed virtual cross-section of the $\text{MoNi}_4/\text{MoO}_2@\text{Ni}$ composite, sample investigated using laboratory nano-XCT. The white regions are MoO_2 micro cuboids. The proposed reconstruction procedure is applied using the FBP algorithm. **a** Prior to the correction procedure, **b** after the beam-hardening correction/intensity adjustment, **c** after detector offset and center of rotation correction, and **d** after final motion compensation

Conclusions

We have demonstrated a systematic approach to determine the 3D morphology of hierarchically structured materials such as electrocatalysts with high accuracy, based on a micro- and nano- X-ray tomography study. The high accuracy of 3D morphological data of the formed micro- and nanostructures is ensured by applying machine learning algorithms for the correction of imaging artefacts of high-resolution X-ray tomography such as beam hardening and for the compensation of

experimental inaccuracies such as misalignment and motions of samples and tool components.

The multi-scale 3D imaging of an electrocatalyst based on XCT, as demonstrated here for a $\text{MoNi}_4/\text{MoO}_2@\text{Ni}$ composite, provides comprehensive 3D information about the hierarchical morphology of the electrocatalyst. This morphology information describes the formed nanostructures, e.g., nanosized particles on supporting structures, and it allows one to increase the total electrochemically active surface area, the number of active

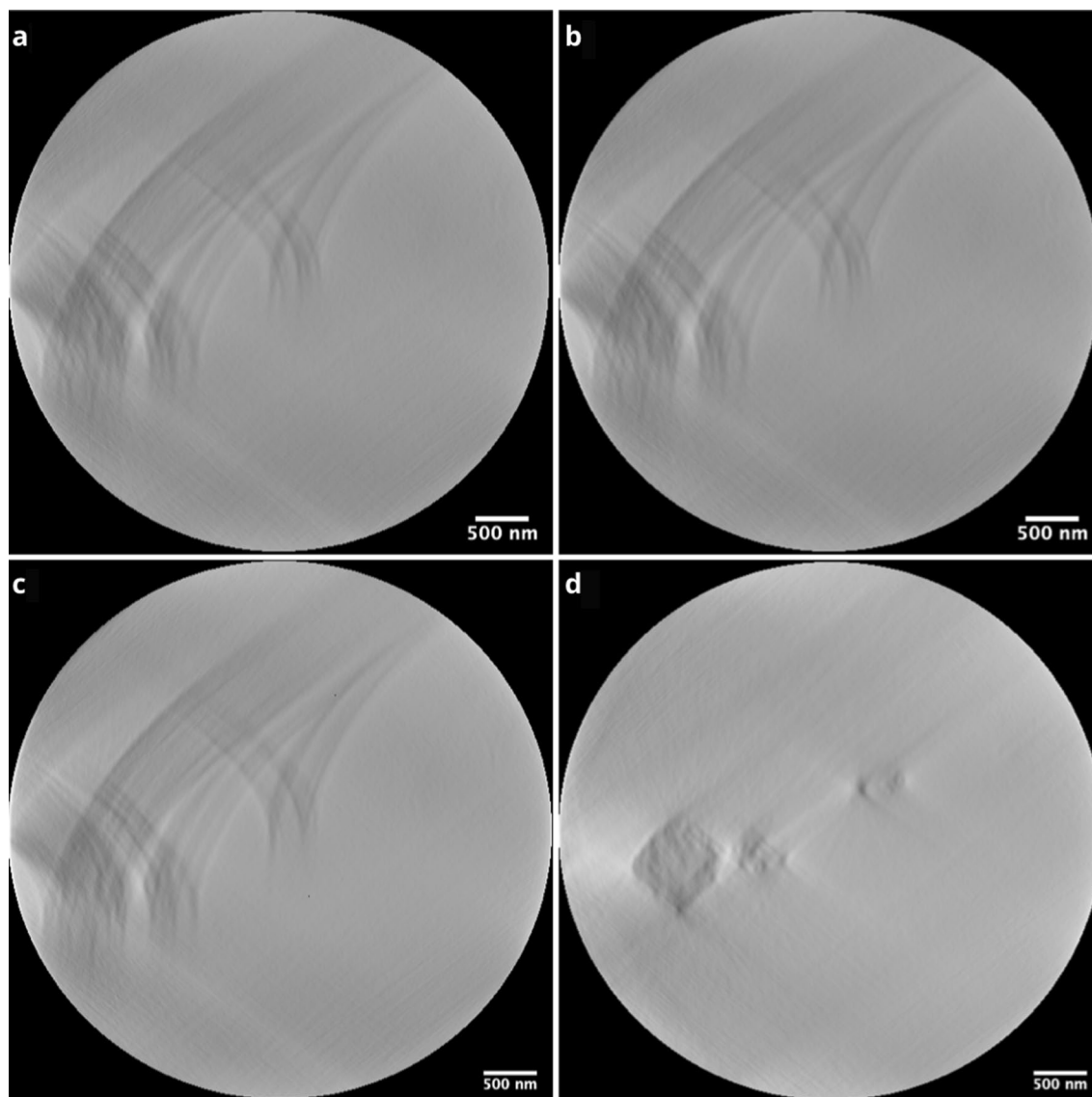
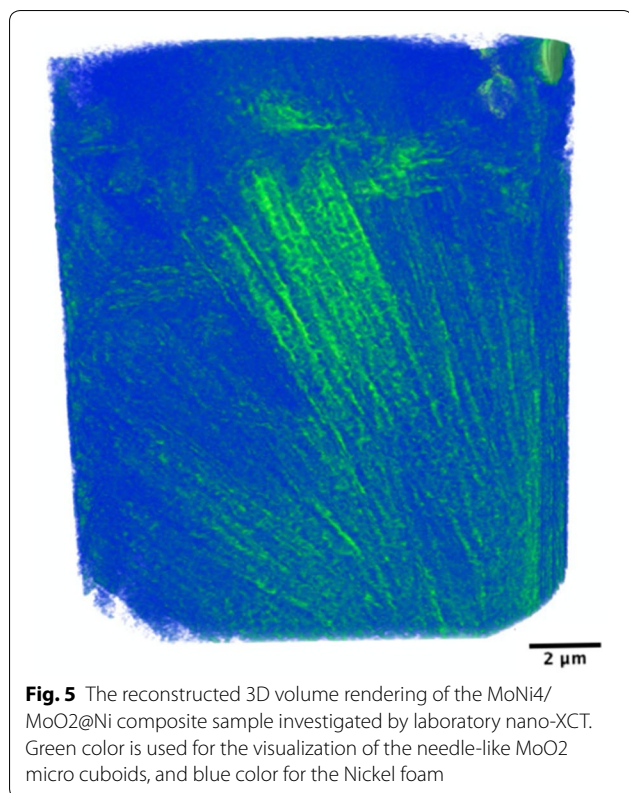


Fig. 4 The reconstructed virtual cross-section of the $\text{MoNi}_4/\text{MoO}_2/\text{Ni}$ composite, sample investigated using synchrotron radiation nano-XCT. The white regions are MoO_2 micro cuboids. The proposed reconstruction procedure is applied using the FBP algorithm. **a** Prior to the correction procedure, **b** after the beam-hardening correction/intensity adjustment, **c** after detector offset and center of rotation correction, and **d** after final motion compensation

catalytic sites, and the ion diffusion (i.e., the reaction rate). This information is complementary to the information about the surface chemistry, i.e., the crystalline structure of the materials and the chemical bonding, which allows one to improve specific surface properties. The morphology information is of particular interest for the up-scaling of processes and for the development of technologies to fabricate advanced energy conversion devices.

Tomography studies, both electron and X-ray, at different scales and with different spatial resolutions, allow to develop, optimize and control the

electrocatalytic processes in devices, particularly substrate and precursor as well as process temperature and time. These parameters have to be balanced to achieve an optimal hierarchical morphology of the electrochemical system, i.e., that the formed nano-sized particles will guarantee an efficient and durable operation during the requested lifetime of an energy conversion device. Particularly, size distribution and shape of cuboids and nano-sized particles can be controlled. Special nanostructures (e.g., arrangements of nanoparticles with optimized size distribution and



porous films) can be developed and characterized to avoid chemical leaching of active species.

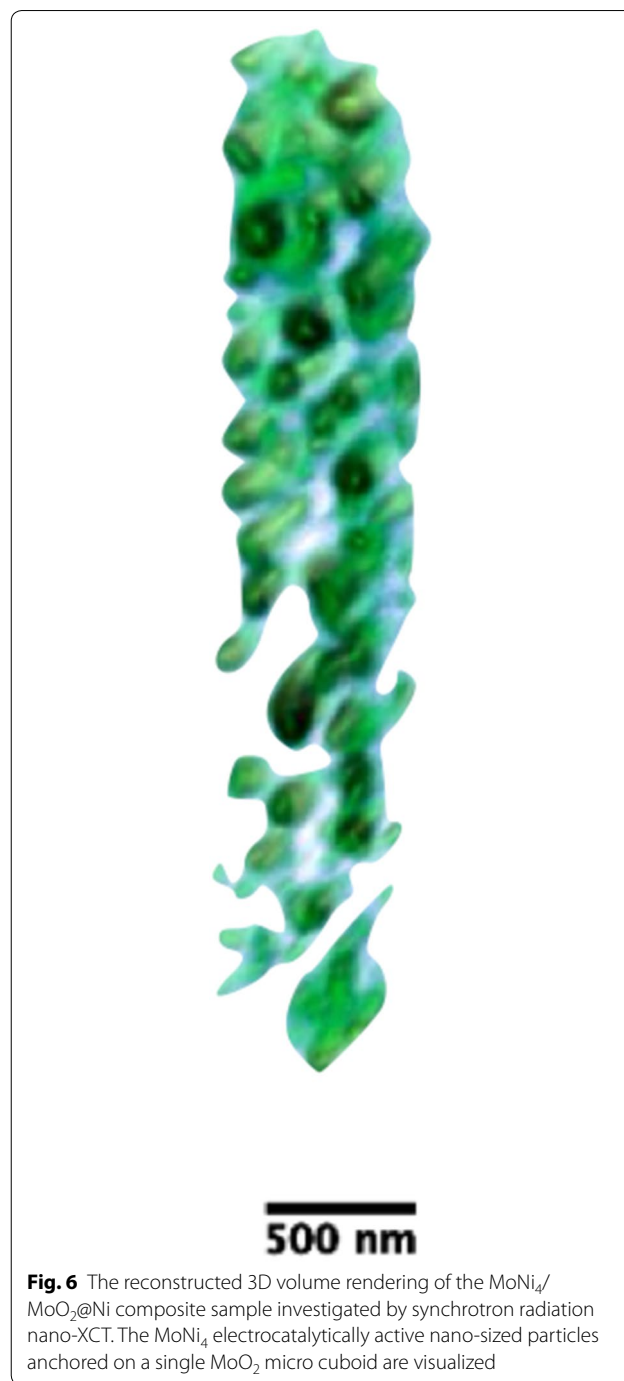
Specially designed operando studies in the TEM or in the XCT tools will provide information about kinetics processes, i.e., the transition of NiMoO₄ cuboids into MoO₂ cuboids and the formation of the nano-sized particles. In addition, degradation processes during operation of catalytic systems, particularly anode electrocatalyst operation at high current density that increases both cell potential and temperature and that causes significant durability issues, can be studied using operando chambers in microscopes that allow one to vary pH value, electrode potential and temperature systematically. In particular, the anodic oxygen evolution reaction is the determining step for the degradation rate of the entire process, and it affects significantly the system stability [38–40].

We believe that our multi-scale tomography study of the 3D morphology of electrocatalysts will open up a new exciting avenue toward exploring the design of robust 3D electrocatalysts with high activity and durability for large-scale hydrogen production.

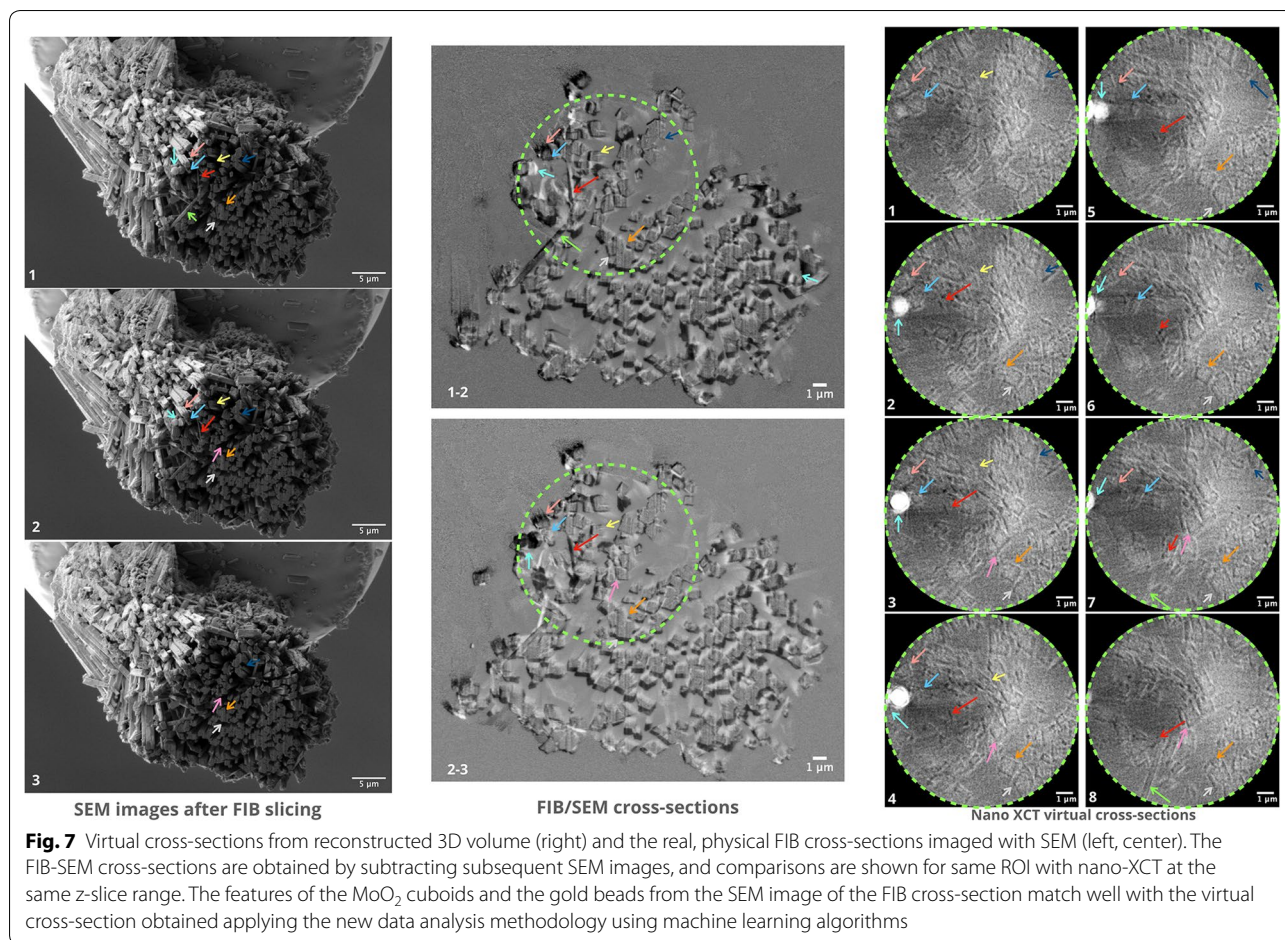
Methods

Synthesis of the MoNi₄/MoO₂@Ni composite

The synthesis of the MoNi₄ electrocatalyst involves two steps (see [6, Fig. 1]). Firstly, NiMoO₄ cuboids



were grown on a piece of Ni foam (1 × 3 cm²) during a hydrothermal reaction at 150 °C for 6 h in 15 ml deionized water containing Ni(NO₃)₂·6H₂O (0.04 M) and (NH₄)₆Mo₇O₂₄·4H₂O (0.01 M). Secondly, while the as-synthesized NiMoO₄ cuboids were heated in a H₂/Ar (v/v, 5/95) atmosphere at 500 °C for 2 h, Ni atoms diffused in a controlled way to the surface of the cuboid and formed numerous MoNi₄ nanoparticles with a size of

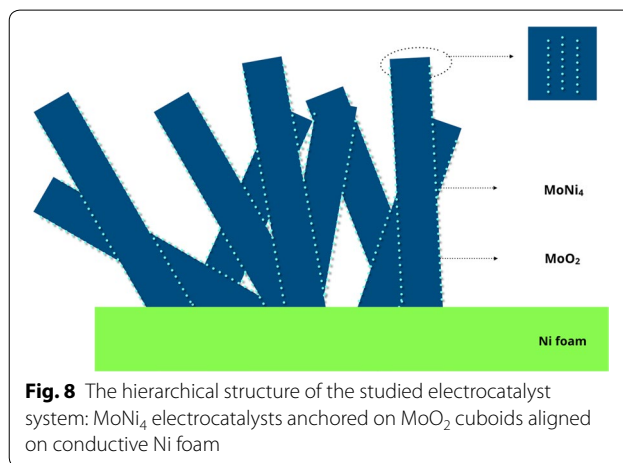


20–100 nm on the surface of the MoO₂ cuboids. Simultaneously, the composition of the cuboids changed from NiMoO₄ to MoO₂ caused by Ni out-diffusion. The MoNi₄ electrocatalyst exhibited a zero onset overpotential, an overpotential of 15 mV at 10 mAcm⁻² and a low Tafel slope of 30 mV per decade in 1 M KOH electrolyte [6].

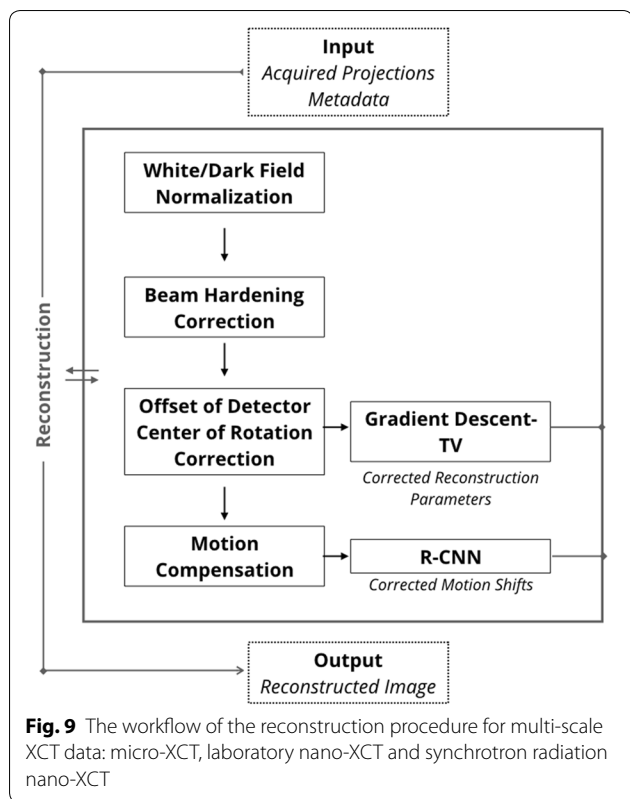
The MoNi₄ electrocatalytically active nano-sized particles anchored on MoO₂ cuboids that are vertically aligned on the conductive Ni foam were characterized using TEM and XPS. In addition, these MoNi₄ nanoparticles and the MoO₂ cuboids were imaged using SEM [6]. A scheme of the hierarchical structure of the system, including Ni foam, MoO₂ supporting cuboids and MoNi₄ nanoparticles is shown in Fig. 8.

Micro-XCT (laboratory tool)

The micro-XCT tool (Zeiss Versa 520) was set to 80 keV: A geometrical magnification of 0.665 and an optical magnification, using an additional scintillator-objective combination in the beam path, of 20.05 resulted in a voxel size of 448 nm. The best possible spatial resolution of the micro-XCT tool is 0.7 μm. A tilt series with 2401 images



was recorded for a complete rotation (angular range of 360°). The exposure time per image was 30 s. This micro-XCT setup uses a cone-beam geometry. The sample was prepared by picking up a loose particle from a section of the Ni support foam with the MoO₂ cuboids and MoNi₄



electrocatalysts on it, and subsequently, it was fixed on the tip. The sample size was about $377 \times 590 \times 365 \mu\text{m}^3$.

Nano-XCT (laboratory tool and synchrotron radiation station)

The laboratory nano-XCT tool (Xradia Ultra 100) was used at a photon energy of 8 keV and in high resolution mode. The spatial resolution of laboratory nano-XCT tool is 50 nm. The field of view was 16 μm with 512 pixels, resulting in a voxel size of 31 nm. A MoO_2 cuboid sample with a size of about $15 \times 15 \times 15 \mu\text{m}^3$ was picked up from the Ni foam scaffold, and subsequently, it was fixed on the tip of a tungsten wire. The tilt series for the tomography consisted of 501 images within an angular range of 180°. The exposure time per image was 265 s. The nano-XCT series conforms to the parallel beam geometry, thus, a half turn is sufficient for a complete tomography.

The synchrotron radiation nano-XCT data were recorded at the BESSY II beamline UX41-TXM at a photon energy of 875 eV. The spatial resolution of the synchrotron radiation nano-XCT tool is 36 nm [41] and achieved voxel size is 9.4 nm. The sample was cleaned in an ultrasonic bath in ethanol, and subsequently, it was dipped on a quantifoil TEM grid. The size of the sample was about $2.4 \times 0.4 \times 0.2 \mu\text{m}^3$. Due to the sample geometry, the tomography tilt series was limited to 110°, with

111 individual images. The exposure time per image was 2 s.

XCT image reconstruction

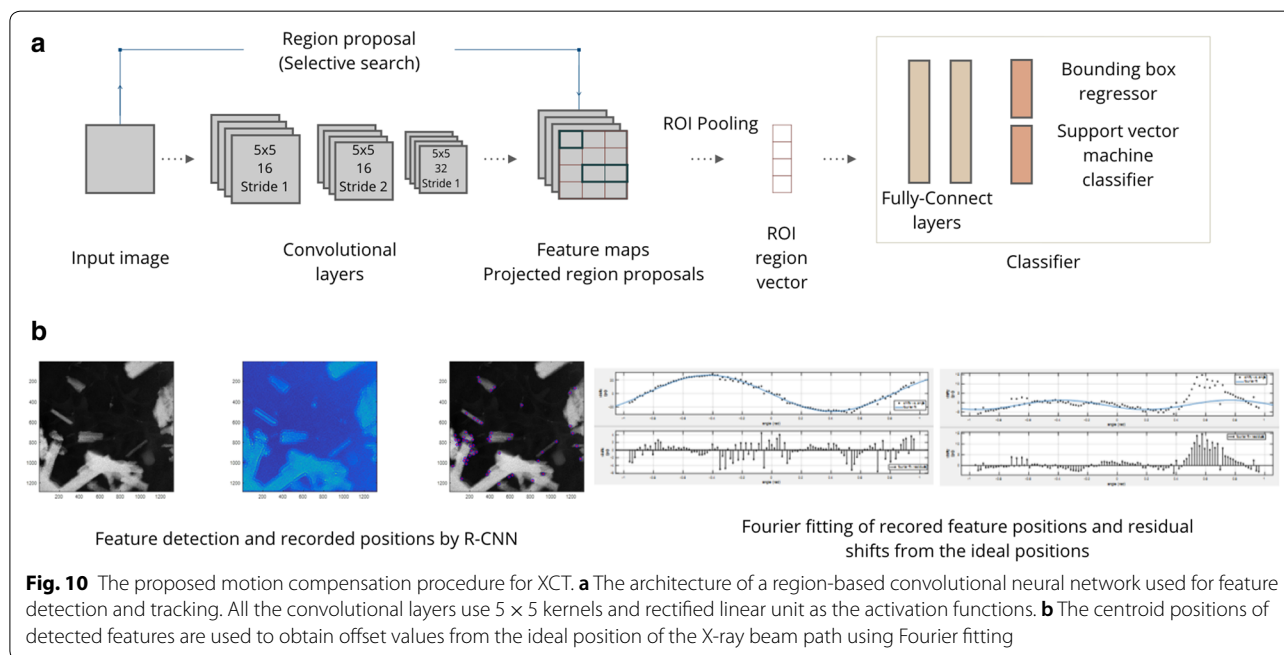
A novel hybrid tomographic image reconstruction approach was developed and implemented for parallel-beam and cone-beam geometries. The proposed hybrid approach includes data driven and machine learning approaches for suppression of artifacts in combination with an analytic image reconstruction algorithm. The procedure followed for the reconstruction of tomographic images is provided in Fig. 9. The applied correction algorithms do not depend on the studied sample volume and the resolution, they are identically for the analysis of the data from all 3 XCT investigations: micro-XCT, laboratory nano-XCT and synchrotron radiation nano-XCT.

The intensities of acquired raw radiographs are initially normalized using Eq. 1:

$$I_{normalized} = \frac{I_{raw} - I_{dark}}{I_{white} - I_{dark}}, \tag{1}$$

The next step is an intensity adjustment to improve the contrast (different grey values) as a part of the beam hardening correction. As one of the most commonly encountered artefacts in X-ray radiography and XCT, beam hardening results in the edges of a homogenous object appearing brighter than the center. Lower energy photons are attenuated more than higher-energy photons, and a polychromatic beam passing through an object preferentially loses its lower-energy part [42]. Ultimately, absorption leads to a diminishment of the overall beam intensity, however, the beam has a higher average photon energy after passing through the object than the incident beam. In order to minimize the artefact, we applied an empirical beam hardening correction approach [43]. The acquired radiographs and the forward projection model are used to derive weight factors for discrete intensity ranges. The obtained weight factors are multiplied with the intensity values of acquired radiographs to suppress beam-hardening artefacts. To adjust the intensities of the multi-scale XCT studies, we applied the beam hardening correction to radiographs from nano-XCT too, even though a monochromatic beam ($\text{Cu-K}\alpha$, 8 keV) is used in this case.

The precise knowledge of the object’s center of rotation with respect to the detector positioning is crucial to obtain an accurate 3D reconstruction from radiographs. The inaccuracy of detector positions has to be taken into consideration during the reconstruction step because systematic ring-like imaging artefacts, introduced by defective and/or underperforming detector elements, appear in the reconstructed images at sharp boundaries. The



correction includes the following steps prior the reconstruction: alignment of the center of sample rotation to the detector grid and compensation of an offset value to compensate detector offset-induced artifacts. To eliminate these artefacts, a reconstruction-based total variation based gradient descent minimization [44] approach is applied. As a result, an estimation of the average detector offset and of the center of rotation is provided applying a multi-range testing approach with a predefined set of values.

The approach used for motion estimation is based on the fiducial marker approach [45], however, the detection and tracking purely relies on intrinsic patterns of the object on two successively acquired 2D tomographic images. We combined computer vision and deep neural network approaches in order to adapt feature tracking to the acquisition procedure of computed tomography data where the features are changing over angles. A region-based CNN (R-CNN) [47] is used for extracting feature maps for detection of intrinsic patterns/features from the acquired projections and for assigning a unique id to each of them. The network design is completed with addition of a Support Vector Machine (SVM) classifier to provide a robust tracking over the entire projections. The architecture of the convolutional neural network for pattern tracking and overview of proposed approach are shown in Fig. 10. The trained model employs a selective search to derive object proposals [46] and extracts region-based convolutional neural network features for each proposal of

possible positions of the feature. It feeds the patterns to a support vector machine classifier to decide if the feature is included in the search windows. Once detection and tracking over projection images is completed, recorded centroid coordinates are fitted accordingly to the position of the center of the X-ray beam to obtain offset values from the ideal position of the X-ray beam path. Eventually, the obtained offset values are used for shifting detector pixel positions in order to compensate motion shifts in reconstructed images. This proposed approach offers clear advantage over the available methods due to fact that it doesn't need prior actions (attaching fiducial marker) and/or post processing (aligning the acquired radiographs according to fiducial marker). Furthermore, the proposed method tracks all the available patterns of the scanned object, and thus, it effectively eliminates errors.

Abbreviations

ORR: oxygen reduction reaction; OER: oxygen evolution reaction; HER: hydrogen evolution reaction; MOFs: metal-organic frameworks; XRD: X-ray diffraction; TEM: transmission electron microscopy; XPS: X-ray photoelectron spectroscopy; XAS: X-ray absorption spectroscopy; BET: Brunauer–Emmett–Teller; SEM: scanning electron microscopy; XCT: X-ray computed tomography; ET: electron tomography; FDK: Feldkamp–Davis–Kress; FBP: filtered back-projection; R-CNN: region-based convolutional neural network; SVM: support vector machine.

Acknowledgements

The authors thank Gerd Schneider, Peter Guttman, Stephan Werner, and Stefan Rehbein, all with Helmholtz Zentrum Berlin, Germany, for their support during the synchrotron radiation experiments at BESSY II.

Authors' contributions

ET performed data processing and wrote and revised the manuscript. ZL, JG, and ML performed experiments and provided the raw data. JZ and XF provided MoNi₄/MoO₂/Ni material system. EZ provided strategic guidance during development of idea, wrote and revised the manuscript. All authors read and approved the final manuscript.

Funding

The authors received no specific funding for this work.

Data and material availability

The datasets generated during and/or analyzed during the current study are available from the corresponding author on reasonable request.

Competing interests

The authors declare that they have no competing interests.

Author details

¹ Center for Advancing Electronics Dresden, Technische Universität Dresden, Dresden, Germany. ² Dresden Center for Nanoanalysis, Technische Universität Dresden, Dresden, Germany. ³ Fraunhofer Institute for Ceramic Technologies and Systems, Dresden, Germany. ⁴ Faculty of Chemistry and Food Chemistry, Technische Universität Dresden, Dresden, Germany.

Received: 12 March 2019 Accepted: 19 February 2020

Published online: 06 March 2020

References

- Vij V, Sultan S, Harzandi AM, Meena A, Tiwari JN, Lee W-G, et al. Nickel-Based Electrocatalysts for Energy-Related Applications: oxygen Reduction, Oxygen Evolution, and Hydrogen Evolution Reactions. *ACS Catal*. 2017;7:7196–225.
- Liu Z-Q, Cheng H, Li N, Ma TY, Su Y-Z. ZnCo₂O₄ quantum dots anchored on nitrogen-doped carbon nanotubes as reversible oxygen reduction/evolution electrocatalysts. *Adv Mater*. 2016;28:3777–84.
- Chen G-F, Ma TY, Liu Z-Q, Li N, Su Y-Z, Davey K, et al. Efficient and stable bifunctional electrocatalysts Ni/NixMy (M = P, S) for overall water splitting. *Adv Funct Mater*. 2016;26:3314–23.
- Subbaraman R, Tripkovic D, Chang K-C, Strmcnik D, Paulikas AP, Hirunsit P, et al. Trends in activity for the water electrolyser reactions on 3d M(Ni Co, Fe, Mn) hydr(oxy)oxide catalysts. *Nat Mater*. 2012;11:550.
- Furukawa H, Cordova KE, O'Keeffe M, Yaghi OM. The chemistry and applications of metal-organic frameworks. *Science*. 2013;341:1230444.
- Zhang J, Wang T, Liu P, Liao Z, Liu S, Zhuang X, et al. Efficient hydrogen production on MoNi₄ electrocatalysts with fast water dissociation kinetics. *Nat Commun*. 2017;8:15437.
- Liu J, Zhu D, Guo C, Vasileff A, Qiao S-Z. Design strategies toward advanced MOF-derived electrocatalysts for energy-conversion reactions. *Adv Energy Mater*. 2017;7:1700518.
- Xu M, Han L, Han Y, Yu Y, Zhai J, Dong S. Porous CoP concave polyhedron electrocatalysts synthesized from metal-organic frameworks with enhanced electrochemical properties for hydrogen evolution. *J Mater Chem A*. 2015;3:21471–7.
- Liu M, Li J. Cobalt phosphide hollow polyhedron as efficient bifunctional electrocatalysts for the evolution reaction of hydrogen and oxygen. *ACS Appl Mater Interfaces*. 2016;8:2158–65.
- Hao J, Yang W, Zhang Z, Tang J. Metal-organic frameworks derived CoxFe_{1-x}P nanocubes for electrochemical hydrogen evolution. *Nanoscale*. 2015;7:11055–62.
- Zhang Y, Xiao J, Lv Q, Wang S. Self-supported transition metal phosphide based electrodes as high-efficient water splitting cathodes. *Front Chem Sci Eng*. 2018;12:494–508.
- Siracusano S, Van Dijk N, Payne-Johnson E, Baglio V, Aricò AS. Nanosized IrOx and IrRuOx electrocatalysts for the O₂ evolution reaction in PEM water electrolyzers. *Appl Catal B Environ*. 2015;164:488–95.
- Rozain C, Mayousse E, Guillet N, Millet P. Influence of iridium oxide loadings on the performance of PEM water electrolysis cells: part II—advanced oxygen electrodes. *Appl Catal B Environ*. 2016;182:123–31.
- Lettenmeier P, Wang L, Golla-Schindler U, Gazzdicki P, Cañas NA, Handl M, et al. Nanosized IrOx-Ir catalyst with relevant activity for anodes of proton exchange membrane electrolysis produced by a cost-effective procedure. *Angew Chem*. 2016;128:752–6.
- Siracusano S, Baglio V, Moukheiber E, Merlo L, Aricò AS. Performance of a PEM water electrolyser combining an IrRu-oxide anode electrocatalyst and a short-side chain Aquivion membrane. 2nd Euro-Mediterr Hydrog Technol Conf EmHyTeC2014 9–12 Dec 2014 Taormina Italy. 2015;40:14430–5.
- Seh ZW, Kibsgaard J, Dickens CF, Chorkendorff I, Nørskov JK, Jaramillo TF. Combining theory and experiment in electrocatalysis: insights into materials design. *Science*. 2017;355:eaad4998.
- Trasatti S. Electrocatalysis by oxides—attempt at a unifying approach. *J Electroanal Chem Interfacial Electrochem*. 1980;111:125–31.
- Rossmesl J, Logadottir A, Nørskov JK. Electrolysis of water on (oxidized) metal surfaces. *Mol Charge Transf Condens Media Phys Chem Biol Nanoeing Honour Alexander M Kuznetsov His 65th Birthd*. 2005;319:178–84.
- Siracusano S, Hodnik N, Jovanovic P, Ruiz-Zepeda F, Šala M, Baglio V, et al. New insights into the stability of a high performance nanostructured catalyst for sustainable water electrolysis. *Nano Energy*. 2017;40:618–32.
- Kumar A, Bhattacharyya S. Porous NiFe-oxide nanocubes as bifunctional electrocatalysts for efficient water-splitting. *ACS Appl Mater Interfaces*. 2017;9:41906–15.
- Xi W, Yan G, Tan H, Xiao L, Cheng S, Khan SU, et al. Superaerophobic P-doped Ni(OH)₂/NiMoO₄ hierarchical nanosheet arrays grown on Ni foam for electrocatalytic overall water splitting. *Dalton Trans*. 2018;47:8787–93.
- Xiao C, Li Y, Lu X, Zhao C. Bifunctional porous NiFe/NiCo₂O₄/Ni foam electrodes with triple hierarchy and double synergies for efficient whole cell water splitting. *Adv Funct Mater*. 2016;26:3515–23.
- Ma TY, Dai S, Qiao SZ. Self-supported electrocatalysts for advanced energy conversion processes. *Mater Today*. 2016;19:265–73.
- Li H, Chen S, Zhang Y, Zhang Q, Jia X, Zhang Q, et al. Systematic design of superaerophobic nanotube-array electrode comprised of transition-metal sulfides for overall water splitting. *Nat Commun*. 2018;9:2452.
- Li Y, Zhang H, Jiang M, Zhang Q, He P, Sun X. 3D self-supported Fe-doped Ni₂P nanosheet arrays as bifunctional catalysts for overall water splitting. *Adv Funct Mater*. 2017;27:1702513.
- Lu Z, Sun M, Xu T, Li Y, Xu W, Chang Z, et al. Superaerophobic electrodes for direct hydrazine fuel cells. *Adv Mater*. 2015;27:2361–6.
- Fang M, Gao W, Dong G, Xia Z, Yip S, Qin Y, et al. Hierarchical NiMo-based 3D electrocatalysts for highly-efficient hydrogen evolution in alkaline conditions. *Nano Energy*. 2016;27:247–54.
- Hu K, Jeong S, Wakisaka M, Fujita J, Ito Y. Bottom-up synthesis of porous NiMo alloy for hydrogen evolution reaction. *Metals*. 2010;8:83.
- Zhao Y, Nakamura R, Kamiya K, Nakanishi S, Hashimoto K. Nitrogen-doped carbon nanomaterials as non-metal electrocatalysts for water oxidation. *Nat Commun*. 2013;4:2390.
- Ahmed MS, Choi B, Kim Y-B. Development of highly active bifunctional electrocatalyst using Co₃O₄ on carbon nanotubes for oxygen reduction and oxygen evolution. *Sci Rep*. 2018;8:2543.
- Yang HB, Miao J, Hung S-F, Chen J, Tao HB, Wang X, et al. Identification of catalytic sites for oxygen reduction and oxygen evolution in N-doped graphene materials: development of highly efficient metal-free bifunctional electrocatalyst. *Sci Adv*. 2016;2:e1501122.
- Friebe D, Louie MW, Bajdich M, Sanwald KE, Cai Y, Wise AM, et al. Identification of highly active Fe sites in (Ni, Fe)OOH for electrocatalytic water splitting. *J Am Chem Soc*. 2015;137:1305–13.
- Banhart J, editor. *Advanced tomographic methods in materials research and engineering*. Oxford, NY: Oxford University Press; 2008.
- Friel J, Quinto ET. Characterization and reduction of artifacts in limited angle tomography. *Inverse Probl*. 2013;29:125007.
- Hsieh J. *Computed tomography: principles, design, artifacts, and recent advances*. 3rd ed. Bellingham, Washington: SPIE; 2015.
- Feldkamp LA, Davis LC, Kress JW. Practical cone-beam algorithm. *J Opt Soc Am A*. 1984;1:612.
- Radon J. On the determination of functions from their integral values along certain manifolds. *IEEE Trans Med Imaging*. 1986;5:170–6.

38. McCrory CCL, Jung S, Peters JC, Jaramillo TF. Benchmarking Heterogeneous Electrocatalysts for the Oxygen Evolution Reaction. *J Am Chem Soc*. 2013;135:16977–87.
39. Katsounaros I, Cherevko S, Zeradjanin AR, Mayrhofer KJJ. Oxygen electrochemistry as a cornerstone for sustainable energy conversion. *Angew Chem Int Ed*. 2014;53:102–21.
40. Chen C-F, King G, Dickerson RM, Papin PA, Gupta S, Kellogg WR, et al. Oxygen-deficient BaTiO_{3-x} perovskite as an efficient bifunctional oxygen electrocatalyst. *Nano Energy*. 2015;13:423–32.
41. Rack A, Zabler S, Müller BR, Riesemeier H, Weidemann G, Lange A, et al. High resolution synchrotron-based radiography and tomography using hard X-rays at the BAMline (BESSY II). *Nucl Instrum Methods Phys Res Sect Accel Spectrometers Detect Assoc Equip*. 2008;586:327–44.
42. Hsieh J, Molthen RC, Dawson CA, Johnson RH. An iterative approach to the beam hardening correction in cone beam CT. *Med Phys*. 2000;27:23–9.
43. Kyriakou Y, Meyer E, Prell D, Kachelrieß M. Empirical beam hardening correction (EBHC) for CT. *Med Phys*. 2010;37:5179–87.
44. Cheng C-C, Ching Y-T, Ko P-H, Hwu Y. Correction of center of rotation and projection angle in synchrotron X-ray computed tomography. *Sci Rep*. 2018;8:9884.
45. Li T, Xing L, Munro P, McGuinness C, Chao M, Yang Y, et al. Four-dimensional cone-beam computed tomography using an on-board imager: 4D on-board CBCT acquisition. *Med Phys*. 2006;33:3825–33.
46. Uijlings JRR, van de Sande KEA, Gevers T, Smeulders AWM. Selective search for object recognition. *Int J Comput Vis*. 2013;104:154–71.
47. Ren S, He K, Girshick R, Sun J. Faster R-CNN: Towards Real-Time Object Detection with Region Proposal Networks. In: Cortes C, Lawrence ND, Lee DD, Sugiyama M, Garnett R, editors. *Advances in Neural Information Processing Systems* 28. Curran Associates, Inc.; 2015. p. 91–99. <http://papers.nips.cc/paper/5638-faster-r-cnn-towards-real-time-object-detection-with-region-proposal-networks.pdf>.

Publisher's Note

Springer Nature remains neutral with regard to jurisdictional claims in published maps and institutional affiliations.

Ready to submit your research? Choose BMC and benefit from:

- fast, convenient online submission
- thorough peer review by experienced researchers in your field
- rapid publication on acceptance
- support for research data, including large and complex data types
- gold Open Access which fosters wider collaboration and increased citations
- maximum visibility for your research: over 100M website views per year

At BMC, research is always in progress.

Learn more biomedcentral.com/submissions

